JOC The Journal of Organic Chemistry

Article

Bond Rotations and Heteroatom Effects in Donor-Acceptor-Donor Molecules: Implications for Thermally Activated Delayed Fluorescence and Room Temperature Phosphorescence

Jonathan S. Ward, Roberto S. Nobuyasu, Mark A. Fox, Andrei S. Batsanov, Jose Santos, Fernando B. Dias, and Martin R. Bryce

J. Org. Chem., **Just Accepted Manuscript** • DOI: 10.1021/acs.joc.8b02187 • Publication Date (Web): 31 Oct 2018

ACS Publications

is published by the American Chemical Society. 1155 Sixteenth Street N.W., Washington, DC 20036

Bond rotations and heteroatom effects in donor-acceptor-donor molecules: Implications for thermally activated delayed fluorescence and room temperature phosphorescence

Jonathan S. Ward,[†] Roberto S. Nobuyasu,[‡] Mark A. Fox,[†] Andrei S. Batsanov,[†] Jose Santos,[†] Fernando B. Dias,[‡] Martin R. Bryce*,[†]

[†] Department of Chemistry, Durham University, Durham, DH1 3LE, UK.

E-mail: m.r.bryce@durham.ac.uk

[‡] Department of Physics, Durham University, Durham, DH1 3LE, UK.

Keywords: TADF, charge transfer, donor-acceptor, emission, phenoxazine

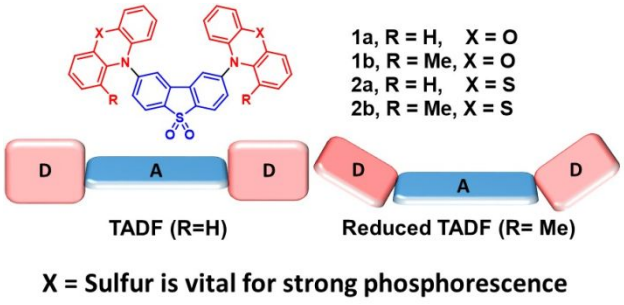

Abstract

The synthesis of 1-methylphenoxazine *via* CO_2-directed lithiation chemistry is reported. This electron donor was coupled with 2,8-dibenzothiophene-*S*,*S*-dioxide with Buchwald–Hartwig chemistry to give a new D–A–D charge-transfer fluorescent molecule **1b**. X-ray crystal structures and calculations show that the phenoxazinyl groups are coplanar and equatorial (eq) to the acceptor plane in non-methylated **1a**, but are pyramidal and axial (ax) in **1b**. The bond rotation energy barriers between donor and acceptor groups for **1a** and **1b** are only 0.13 and 0.19 eV respectively from hybrid-DFT computations at the CAM-B3LYP/6-31G(d) level. Many possible conformers are present in solutions and in zeonex. In zeonex, the

methyl groups in **1b** shift the emission band 0.13 eV higher in energy compared to **1a**. Excited state eq-eq and ax-ax geometries were identified with DFT calculations, with charge transfer (CT) emission assigned as ^{1}CT(eq) and ^{1}CT(ax) dominating. The lower energy ^{1}CT(eq) contributes to thermally activated delayed fluorescence (TADF), whereas the higher energy ^{1}CT(ax) does not. Phenothiazine analogs **2a** and **2b**, also have major fluorescence emissions assigned as ^{1}CT(eq) and ^{1}CT(ax) respectively. **2a**-**b** have substantial room temperature phosphorescence (RTP) whereas **1a-b** do not, highlighting the importance of the sulfur atom in **2a-b** to obtain RTP emission.

Introduction

Luminescent aromatic and heteroaromatic organic molecules are widely used in many modern applications including organic light emitting diodes (OLEDs),[1-3] solar cells,[4,5] bio-imaging,[6] security,[7,8] and sensing.[9,10] In particular, organic molecules are prime candidates for OLED applications with the photoluminescence quantum yields reaching 100%.[11,12] By reducing non-radiative decay, most of the excited states that form in a device can emit, thus enhancing their performance.

Harvesting triplet excited states requires strategic molecular design, notably by employing electron donor-acceptor (D−A) molecules with a degree of conjugational isolation between the D and A fragments to reduce the singlet-triplet gap.[1,13-22] This occurs due to localized triplet states (^{3}LE) originating from the donor or acceptor having similar energy to the singlet charge transfer state (^{1}CT). When the low energy singlet and triplet states are close in energy (within two or three times k_BT at ambient temperature), selection rules are relaxed and reverse intersystem crossing (RISC) can occur at a fast rate (10^4 – 10^7 s^{-1}).[23] Harvesting triplet states by a thermally activated RISC mechanism is termed thermally activated delayed fluorescence (TADF). This process has propelled the efficiency of OLED devices by several fold compared with standard organic fluorescent emitters.[19] RISC allows for harvesting of the 75% triplet excited states formed during electrical excitation, and their conversion into singlet states. These states can then emit rapidly, and this has resulted in OLEDs with >30% external quantum efficiency (EQE).[19]

Recent research has significantly improved the understanding of the triplet harvesting processes, but the detailed mechanism by which this occurs is not yet completely understood.[24-28] Further investigations are therefore needed for the development of next generation materials.

Phenoxazine is a known building block in TADF systems.[29-31] Here, D−A−D molecules **1a** and **1b**, with phenoxazine and 1-methylphenoxazine donors, respectively, in combination with a dibenzothiophene-*S,S*-dioxide acceptor are investigated (**Figure 1**). Compound **1a** has been reported previously to have delayed fluorescence (DF).[29] Through a detailed comparison of **1a** and **1b**, we demonstrate that changes in the D−A−D molecular structure have a drastic impact on the photophysical properties. The structures of **1a** and **1b** were determined by single crystal X-ray diffraction and revealed very different conformers.

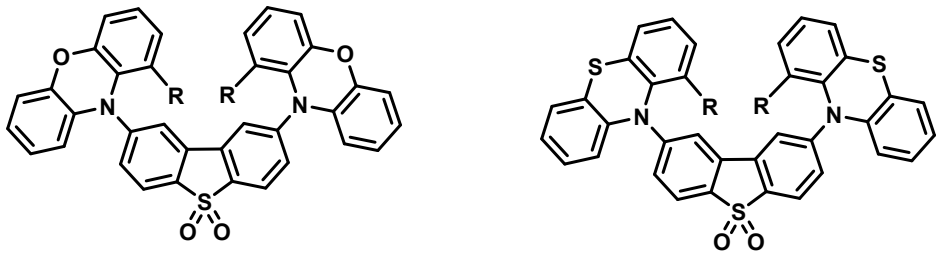

Figure 1. D–A–D molecules discussed in this work.

Here, compounds **1a** and **1b** in zeonex are studied in detail by steady state, time-delay and low temperature emission spectroscopy techniques. The use of zeonex, rather than solvents or crystals, in photophysical measurements is important for OLEDs where the emitter is usually fabricated in a solid state film (layer). The zeonex matrix is a hydrophobic aliphatic polymer with no electronic absorptions in the visible region. Molecules in a zeonex film are spaced out by the inert matrix and therefore are highly unlikely to exhibit any excimer/exciplex type emission. This simplifies the interpretation of emission measurements, by eliminating intermolecular contributions. These studies, in combination with calculations, contribute significantly to explaining how conformers affect the complex photophysics of

TADF molecules. Specifically, TADF is reduced in **1b** due to the methyl groups inducing contributions from geometries in zeonex that forbid the RISC process.

The present work was inspired by recent studies of a series of D−A−D molecules with phenothiazine donor units.[21,32,33] Phenothiazine analogues of **1a** and **1b** are depicted as **2a** and **2b** respectively (**Figure 1**). Compound **2a** (known as **DPTZ-DBTO2**) has been shown to be an efficient TADF emitter in methylcyclohexane, zeonex and other hosts.[22] However, when 1-methyl substituents are added to the phenothiazine units as in **2b**, TADF was absent in zeonex and room-temperature phosphorescence (RTP) was observed.[21]

Results and discussion

While compound **1a** was easily made from phenoxazine **3** as described in the literature,[34] the synthesis of **1b** shown in **Scheme 1** required a more complex methodology. There is currently only one reported route to 1-alkylphenoxazine derivatives without other substituents on the ring system.[35] Katritzky and co-workers reported that the C(1) of intermediate **4** could be deprotonated with assistance from the adjacent $–CO_2Li$ group. This gives access to the dilithiated species **5** that upon reaction with electrophiles gave a range of 1-substituted phenoxazines, although 1-methylphenoxazine **6** was not reported.[35]

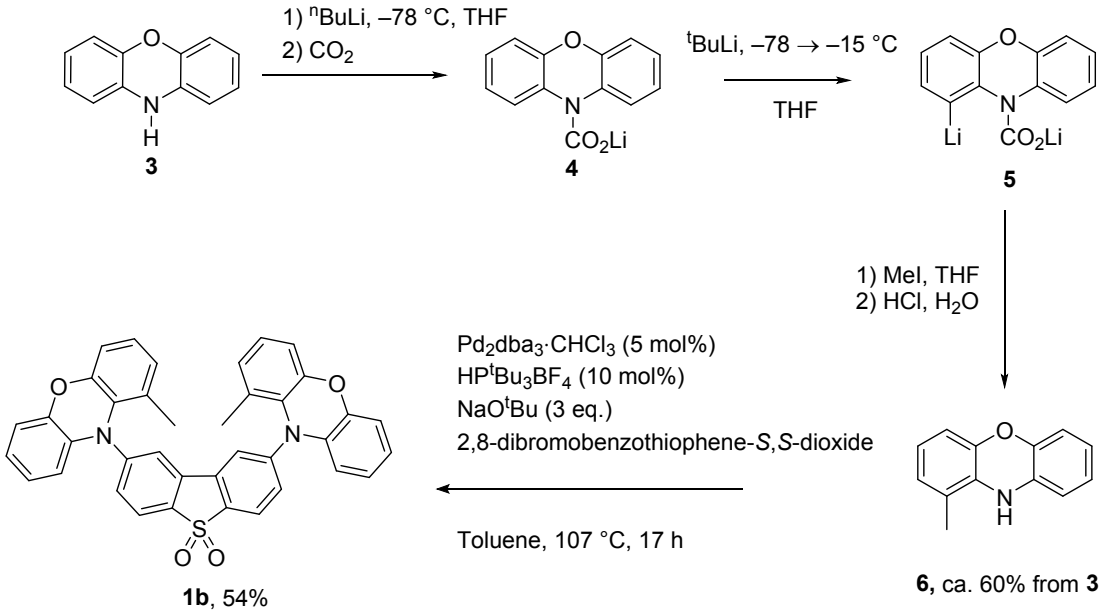

Scheme 1. The synthetic route to **1b**.

The lithiation and methylation of the 1-position of phenoxazine **3** are very sensitive to the reaction conditions, and required the sequential use of 1.0 equivalent of ^{t}BuLi and MeI. A small amount (≈5%) of unreacted **3** could not be separated from **6**. The use of 1.25 equivalents of ^{t}BuLi and MeI gave a by-product which appeared by ASAP-MS analysis to be a dimethylated phenoxazine derivative (<5% by ^{1}H NMR analysis of the crude product mixture) which could also not be separated from **6** (**Figures S1a**, **S1b**). Pleasingly, in the Buchwald-Hartwig coupling reaction of **6** (containing ≈5% of **3**) with 2,8-dibromodibenzothiophene-*S,S*-dioxide the side-products formed in this reaction were easily separated from **1b** by column chromatography, to give pure **1b** (**Figures S1c**, **S1d**) in 54% yield.

Crystal structures of **1a** and **1b** shown in **Figure 2** reveal different conformers as equatorial-equatorial (eq-eq) and axial-axial (ax-ax) respectively. Axial and equatorial are defined as previously reported in the literature.[36] The molecule of **1a** lies astride a crystallographic mirror plane which passes through the sulfone and is perpendicular to the planar dibenzothiophene system. The phenoxazine donors are also planar and inclined by 78° to the dibenzothiophene plane and by 79.5° to one another. Molecule **1b** has no crystallographic symmetry. Its dibenzothiophene system is also nearly planar, with a 3.2° twist

between arene rings, but in contrast to **1a**, both phenoxazine moieties are folded along the N→O vectors, forming dihedral angles of 143.3° and 144.4°. In **1a**, the N atom is trigonal planar and participates in the phenoxazine π-system, while conjugation to the dibenzothiophene is precluded by the twisted conformation. In **1b**, the N atoms are substantially pyramidal: the sum of bond angles at N(1) and N(2) are 353° and 348°, respectively. The N lone pairs can interact with the π-orbitals of dibenzothiophene (torsion angles 17–19°), but not with those of the phenoxazine arene rings (torsion angles 57−62°). Thus, N-C(phenoxazine) bond distances in **1a** are shorter than N-C(dibenzothiophene), 1.401(2) *vs.* 1.430(2) Å, whereas in **1b** it is reversed, 1.436(3) vs. 1.415(3) Å.

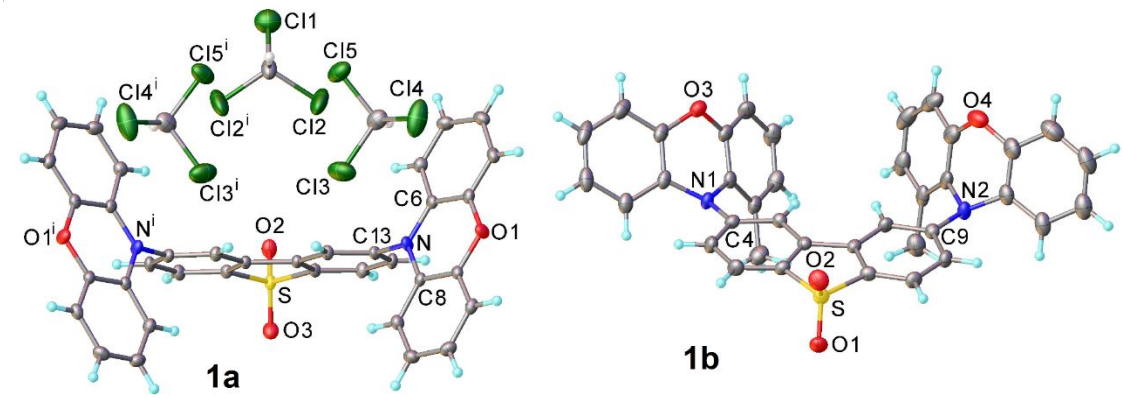

Figure 2. X-ray molecular structures of **1a**·3$CDCl_3$ (eq-eq conformer) and **1b** (ax-ax conformer). Atomic displacement ellipsoids are drawn at the 50% probability level. Primed atoms are generated by the mirror plane. Minor orientations of the disordered $CDCl_3$ are omitted for clarity.

A survey of the Cambridge Structural Database[37] (version 5.38) shows that *N*-substituted phenoxazines are conformationally rather flexible. In the eighteen structures where the substituent is an arene (as in **1a-b**), the phenoxazine moiety is usually near-planar. Although foldings with the dihedral angles of 162° and 156° have also been observed,[38,39] the near-orthogonality and non-conjugation with the arene substituent is always maintained. In the nine available structures with –C(=O)R substituents, the phenoxazine unit is always folded (dihedral angles 141−152°) and there is N-C-O conjugation. Thus, the methyl substituent on the phenoxazine in **1b** forces the latter type of conformation and corresponding π-

delocalization mode, which should have significant effects on the photophysical properties of **1b** compared to **1a**. The absorption spectra of **1a** and **1b** in dichloromethane solution reveal lowest energy band cut offs at 525 and 410 nm, respectively (**Figure S2a**). The energy difference of 0.66 eV between these values suggests that the HOMO-LUMO energy gap (HLG) for **1b** is larger than for **1a**, which may be attributed to the different nitrogen environments and conformations between these molecules.

Cyclic voltammetry (CV) measurements on **1a** and **1b** were carried out to obtain oxidation and reduction potentials and hence the estimated HOMO and LUMO levels (**Tables 1, S1 and S2, Figures S3a-d**). CH_2Cl_2 was first used as solvent for the measurements but the reduction wave of **1b** was close to the reduction of the solvent (**Figure S3b**). Dimethylformamide (DMF) was found to be a more suitable solvent for the chemically reversible oxidation and reduction waves of **1b** (**Figure S3a**). No change in the CV trace was observed after three cycles thus establishing the high stability of the oxidized and reduced species of **1b**. The solvent DMF was also used for CV measurements of **2a** and **2b** here for direct comparison with the phenoxazines (**Figure S3c**). However, the oxidation wave for **2b** in DMF was not reversible thus the oxidized species of **2b** is not stable in DMF. From **Table 1**, the methyl groups of **1b** and **2b** raise the LUMO energies and lower the HOMO energies by a similar energy value with respect to its corresponding parent systems **1a** and **2a**. The HOMO-LUMO energy gap (HLG) increases by 0.31 eV on going from **1a** to **1b** whereas it increases by 0.71 eV from **2a** to **2b**. The increase in the HLG from **1a** to **1b** is in accord with the absorption data for **1a** and **1b** (**Figure S2a**).

Table 1. MO energies determined from CV measurements in DMF.

	HOMO eV	LUMO eV	HLG eV
1a	−5.37	−3.09	2.28
1b	−5.52	−2.93	2.59
2a	−5.39	−3.06	2.33
2b	−5.75	−2.71	3.04

Hybrid DFT calculations were performed to examine which conformers are likely to be present for **1a** and **1b** in solutions and in zeonex. Ground state geometry optimizations on all possible conformers for **1a** and **1b** revealed that all conformers were located as minima except for two in the case of **1b**. In **1a**, four minima were located, namely eq-eq, eq-ax, ax-ax (*trans*) and ax-ax (*cis*) (**Figure S4a**) with eq-eq as the most stable geometry as found in the X-ray crystal structure for **1a** (**Figure 2**). The experimental and computed geometric parameters are in very good agreement (**Table S3**). This gives confidence in CAM-B3LYP/6-31G(d) as an appropriate model chemistry for D–A–D systems in **Figure 1**. The eq-ax conformer of **1a** is 0.07 eV higher in energy than the eq-eq conformer, thus it would represent ca. 5% of the conformer distribution of **1a** in solution or in zeonex at room temperature. The ax-ax conformers of **1a** are over 0.20 eV higher in energy compared to the eq-eq conformer, thus there would be only trace quantities of the ax-ax conformers at room temperature.

The rotation barrier between eq-eq and eq-ax conformers was estimated by fixing the C(donor)-N(donor)-C(acceptor)-C(acceptor) torsion angle between one donor group and the acceptor moiety. Each geometry was optimized with the CNCC torsion angle as the only constraint. The torsion angle was changed in five-degree intervals to give a relative rotation energy profile in **Figure 3**. The ax conformation would have a CNCC torsion angle of about 15^{o}. In contrast the eq conformation would have a CNCC torsion angle of about 75^{o} when the donor group is folded, and about 85^{o} when the donor group is planar. The rotation barrier is only 0.13 eV for **1a**, which suggests that both conformers interconvert in solution at room temperature.[40] On fabrication of a solid zeonex film with evaporation of the solvent, it is proposed that conformers in solution are 'trapped' in the zeonex matrix, and cannot convert once in the solid matrix.

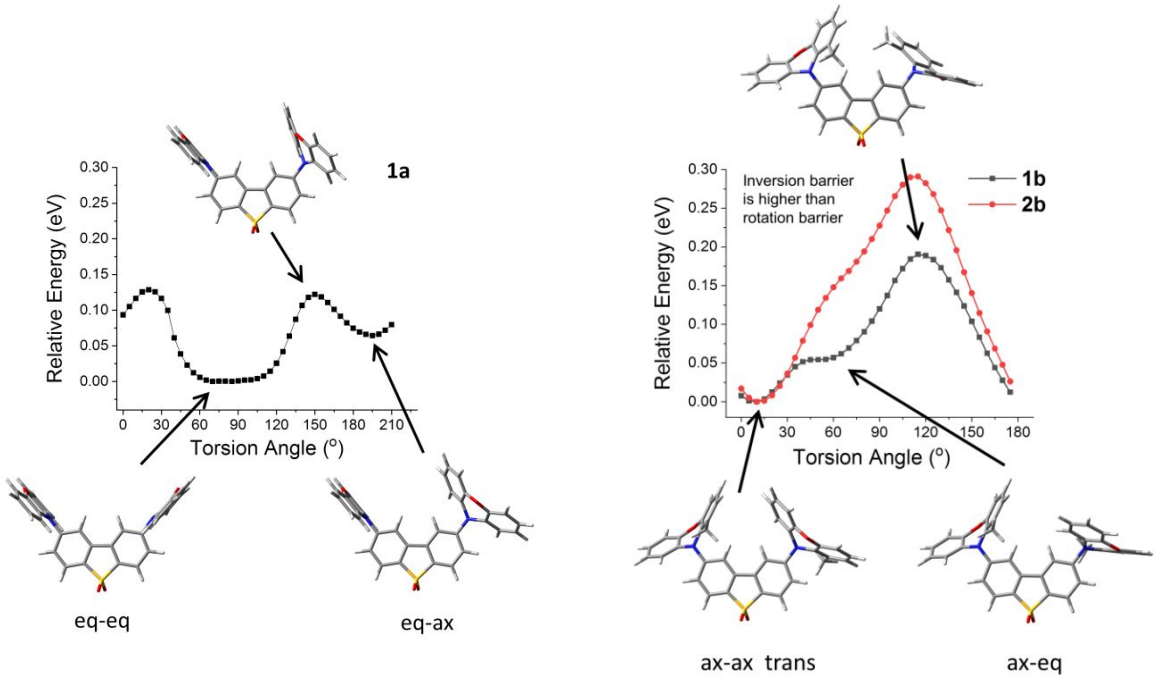

Figure 3. Rotation energy profiles for **1a** (left) and **1b** (right) calculated at CAM-B3LYP/6-31G(d) level with geometries at selected maximum and minimum points shown. The profile for **2b** is included in the **1b** plot for direct comparison with **1b**.

While there is a clear conformer preference for **1a**, the relative energies for the eighteen different conformer minima located for **1b** are less than 0.1 eV apart (**Figure S4b**). The ax-ax conformers are most likely to be present with the ax-eq conformers some 0.03 eV higher in energy and the eq-eq conformers a further 0.06 eV higher. An ax-ax:ax-eq:eq-eq population ratio of 80:19:1 is predicted for **1b** in solutions and in zeonex at room temperature. The rotation energy profile for **1b** in **Figure 3** between ax-ax and ax-eq conformers shows a rotation barrier of only 0.19 eV meaning that interconversions between these conformers exist in solutions at room temperature. By constraining the NC_6H_4O ring to be planar and optimizing the geometry of **1b**, the inversion barrier at N in **1b** is estimated at 0.21 eV. This value is slightly higher than the rotation barrier. Nevertheless at room temperature interconversion of the stereoisomers in **1b** would occur. For **1a** and **1b**, the geometry calculations show that the barriers between

the ax-eq conformers and other minor conformers are very low in solution. The ^{1}H peaks in the NMR spectra (**Figure S1c**) are sharp for each environment, strongly suggesting that the peaks observed are averaged from rapid interconversions of many different conformers in solutions.

Simulated absorption spectra from the most stable conformers of **1a** and **1b** show similarities with observed absorption spectra (**Figure S2b**). The large energy difference of 0.66 eV observed between the lowest energy bands is correctly reproduced by computations with a value of 0.70 eV. The simulated spectra are based on static gas-phase geometries of the eq-eq conformer of **1a** and the ax-ax conformer of **1b** rather than an averaged mixture of conformers of **1a** and **1b**. Nevertheless, the data shows that different conformations in these D–A–D systems relate to corresponding lowest energy transitions.

The phenothiazines, **2a** and **2b**, were also subjected to detailed computations at CAM-B3LYP/6-31G(d) level here for comparison with **1a** and **1b**. There are crystallographic reports of **2a** where both ax-ax and eq-eq conformers were determined.[22,29,41] These studies suggest that any conformer of **2a** exists depending on the surrounding environment and these distinct conformers are similar in energy. Here, the ax-ax and ax-eq conformers of **2a** were essentially identical in energies (**Figure S4c**). The eq-eq conformers were 0.06-0.09 eV higher in energies. These values suggest an ax-ax:ax-eq:eq-eq population ratio of 48:48:4 in solutions and in zeonex at room temperature, which is clearly different to **1a** where a 0:5:95 ratio is predicted. The rotation energy profile for **2a** is complicated by the preference for the pyramidal environment at N in all conformers as shown in **Figure 4**. The inversion barrier at N of 0.10 eV in **2a** is lower than the rotation barrier of 0.13 eV. Therefore, inversion at N can take place when optimizing a geometry with a fixed torsion angle in order to lower the energy of the constrained geometry. The low rotation energy barriers suggest all conformers of **2a** interconvert in solutions at room temperature. On fabrication of a solid zeonex film of **2a** with evaporation of the solvent, the conformers would be 'trapped' in the zeonex matrix mainly as the ax-ax and ax-eq forms.

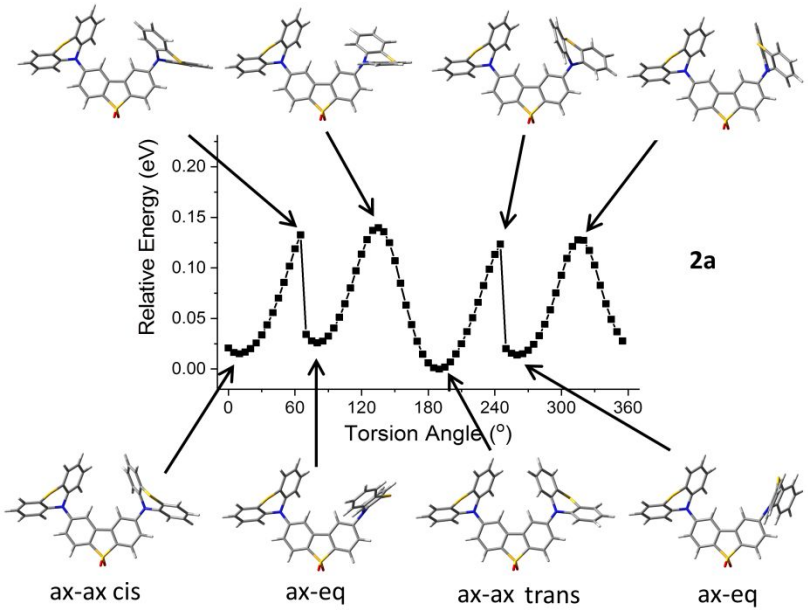

Figure 4. Rotation energy profiles for **2a** at CAM-B3LYP/6-31G(d) with geometries at selected maximum and minimum points shown.

In the computational study of the ground state geometries of **2b**, interestingly only the ax-ax conformers could be located as minima. This is in contrast to **1a**, **1b** and **2a** where all three distinct ax-ax, ax-eq and eq-eq conformers could be located as minima (**Figure S4c**). The rotation energy profile for **2b** in **Figure 3** shows a strong energetic preference for the ax-ax conformer and the estimated rotation barrier is high at 0.29 eV; nevertheless there should be free rotations in solutions of **2b** at room temperature. The inversion barrier at N in **2b** is even higher at 0.60 eV. The ax-ax conformers would only be present for **2b** in zeonex and probably in the solid state. An ax-ax conformer of **2b** has been determined by X-ray crystallography elsewhere.[41]

HOMO and LUMO energies from electronic structure calculations on selected minima of **1a**, **1b**, **2a** and **2b** at CAM-B3LYP/6-31G(d) suggest that methyl groups subtly lower the HOMO energies and raise the LUMO energies between the same conformers (**Table S4**). For example, computed HOMO energies for ax-ax conformers of **1a**, **1b**, **2a** and **2b** are −5.84, −5.92, −5.84 and −5.90 eV respectively. However, the HOMO and LUMO energy differences between ax-ax and ax-eq conformers are more pronounced where,

for example, the HOMO energies of ax-eq and the ax-ax conformers of **1a** are −5.26 and −5.84 eV respectively. The HLG energies therefore increase markedly on going from the ax-eq conformer to the ax-ax conformer irrespective of the presence or absence of the methyl groups. Based on the observed CV data in **Table 1**, it may be assumed that the ax-ax conformer is dominant in DMF or CH_2Cl_2 solutions of **2b**, whereas for **1b** there are substantial ax-ax conformers in DMF or CH_2Cl_2 solutions with the larger HLG energies of 3.04 and 2.59 eV for **2b** and **1b** respectively. The conformations in these D–A–D systems therefore influence the frontier orbital energies far more than the electronic effects of the methyl groups.

The computations so far demonstrate how several different conformers exist in solution for **1a** and **1b** and that these would be 'locked' when fabricated into solid thin films. Detailed emission measurements were carried out on **1a** and **1b** in zeonex here in order to identify the different emissions arising from different conformers with the aid of excited state geometry calculations. Such emission data are compared with reported data for **2a** and **2b** in zeonex to assign the multiple emissions for the latter phenothiazines.

The steady state emission spectra for all four D–A–D systems in the absence of oxygen differ from the steady state emission spectra in the presence of oxygen in **Figure 5**. These differences mean the emission quenched by oxygen could originate from an excited state that was at some point in its lifetime in the triplet excited state, but could convert to a singlet state before emitting. For **1a**, the nearly identical shape of both bands in the presence and absence of oxygen means that only TADF is present in **1a** along with prompt fluorescence of the same transition (see normalized spectra in **Figure S5e**). The oxygen-dependent emission intensity ratio was determined from the integral of the emission spectra with and without oxygen[23] and this ratio is independent of wavelength. This ratio [I(no O_2):I(O_2)] is 6.28:1 for **1a**. By contrast, there is very little change in the spectra for **1b** in the absence and presence of oxygen with an intensity ratio of 1.08:1. The emission for **1a** and **1b** contains no phosphorescence (PH) at 290 K in the absence of oxygen, thus the oxygen dependence of the emission is independent of wavelength. This is clarified by the normalization of spectra in **Figure S5e**. In contrast for **2a** there is a new emission band

appearing on removal of oxygen resulting in a blue-shift of the emission spectrum. For **2b** there is a subtle red shift with increased vibronic character due to the increased rigidity of the molecule. The changing spectral profiles on removal of oxygen for **2a** and **2b** are due to room temperature phosphorescence, and explains why the oxygen dependence is wavelength dependent for **2a-b**. The emission spectrum of **1b** is mostly prompt fluorescence. However, the vestigial amount of delayed emission from **1b** that is dependent on oxygen and temperature (**Figure 5+Figure S5c+e)** is assigned as TADF emission. The decays in **Figures S5b-c** show clearly prompt fluorescence and delay fluorescence components, identified by the two exponential profiles appearing at very different delay times, and phosphorescence, which is identified by a clear change in spectral shape and energy occurring at longer delays. The temperature dependence observed between 100 ns and 3 ms is due to the signature of TADF. As the RISC rate measuring the upconversion of triplet states to the singlet manifold, decreases exponentially with temperature, less delayed fluorescence is observed at low temperatures, as expected. The photoluminescence quantum yields (PLQYs) for **1a** and **1b** in zeonex are 42(±6) and 19(±6)% respectively, therefore non-radiative pathways dominate in these systems.

Comparison of the steady state emission spectra for **1a** and **1b** shows that the methyl groups in **1b** blue-shift the fluorescence emission wavelength at room temperature by 0.13 eV in **1b** compared to **1a** (**Figures 5** and **S5a**). The phosphorescence spectra at 77 K also reveal a similar blue-shift of the lowest triplet level in **1b** by 0.08 eV compared to **1a** (**Figure S5a**). The phosphorescence emission band at 77 K for **1a** is broad whereas for **1b** it exhibits vibronic structure. The vibronic structure of the delayed emission spectrum in **1b** at 77 K (**Figure S5a**) is clear, and the fact that it is observed at 77 K, a temperature where TADF is unlikely to be observed in most compounds, and with a much longer lifetime (50 ms) strongly indicates this spectrum to be solely due to PH. The singlet-triplet gap (ΔE_{ST}) was determined from the onsets of delayed fluorescence spectra and low temperature phosphorescence spectra with 50 ms time delay to obtain the energy levels for the 0-0 transitions (**Figure S5a**). The ΔE_{ST} values for **1a** and **1b** are 0.06 and 0.04 eV respectively, which are very small, explaining the efficient TADF

observed in **1a**. The ΔE_{ST} from delayed emission measurements does not explain why **1b** has such low TADF contributions. This can be explained by the domination of the phenoxazine axial conformation in **1b** with higher energy charge-transfer axial emission compared to equatorial (2.91 eV vs 2.79 eV for eq. determined from **Figure S5a**). **1a** does not have any axial contributions to the emission hence the efficient TADF emission. The eq and ax conformations of **1b** have different ΔE_{ST} values (0.04 eV *vs.* 0.16 eV), and this explains the low TADF contributions from **1b**. All of this information has been summarized in **Table 2** below.

Table 2. Absorption and emission photophysical parameters for **1a** and **1b** in zeonex matrix

Entry	λ_{max} abs (nm) [a]	ε (dm^3 mol^{-1} cm^{-1})[b]	λ_{max} em (nm)	Φ_{em} ± 6%	Em onset eV (nm)[c]	$^1CT_{(ax)}$ eV (nm)[d]	$^1CT_{(eq)}$ eV (nm)[d]	T_1 eV (nm)[e]	$\Delta E_{ST(ax)}$ (eV)	$\Delta E_{ST(eq)}$ (eV)
1a	398	2567	494	42	2.81 (441)	-	2.73 (454)	2.67 (465)	-	0.06
1b	328	19734	491	19	2.94 (422)	2.91 (426)	2.79 (443)	2.75 (448)	0.16	0.04

[a] Lowest energy band reported
[b] Co-efficient for the λ_{max} abs shown
[c] Measured from onset of the main emission band in the steady state emission
[d] Determined from the time-jump data using onsets of the assigned CT emission band (**Figure S5a-d**). note: **1a** does not contain any CT (ax) emission.
[e] Determined from the onset of the phosphorescence emission at 77 K with 2 ms delay-time and 50 ms of integration time.

The room temperature steady state emission spectra for **2a**[22] and **2b**[21] in the presence and absence of oxygen are included here for comparison (**Figure 5**). Like **1a**, there is a large effect on the emission spectrum for **2a** when oxygen is present with an intensity ratio of 6.50:1. Unlike **1a**, the band shape in both spectra of **2a** is different which is ascribed to phosphorescence as well as TADF present in **2a**. Emission from **2b** is highly dependent on oxygen, with an intensity ratio of 2.43:1, and can be assigned to room temperature phosphorescence (RTP) due to the clearly defined vibronic structure observed only in the absence of oxygen.

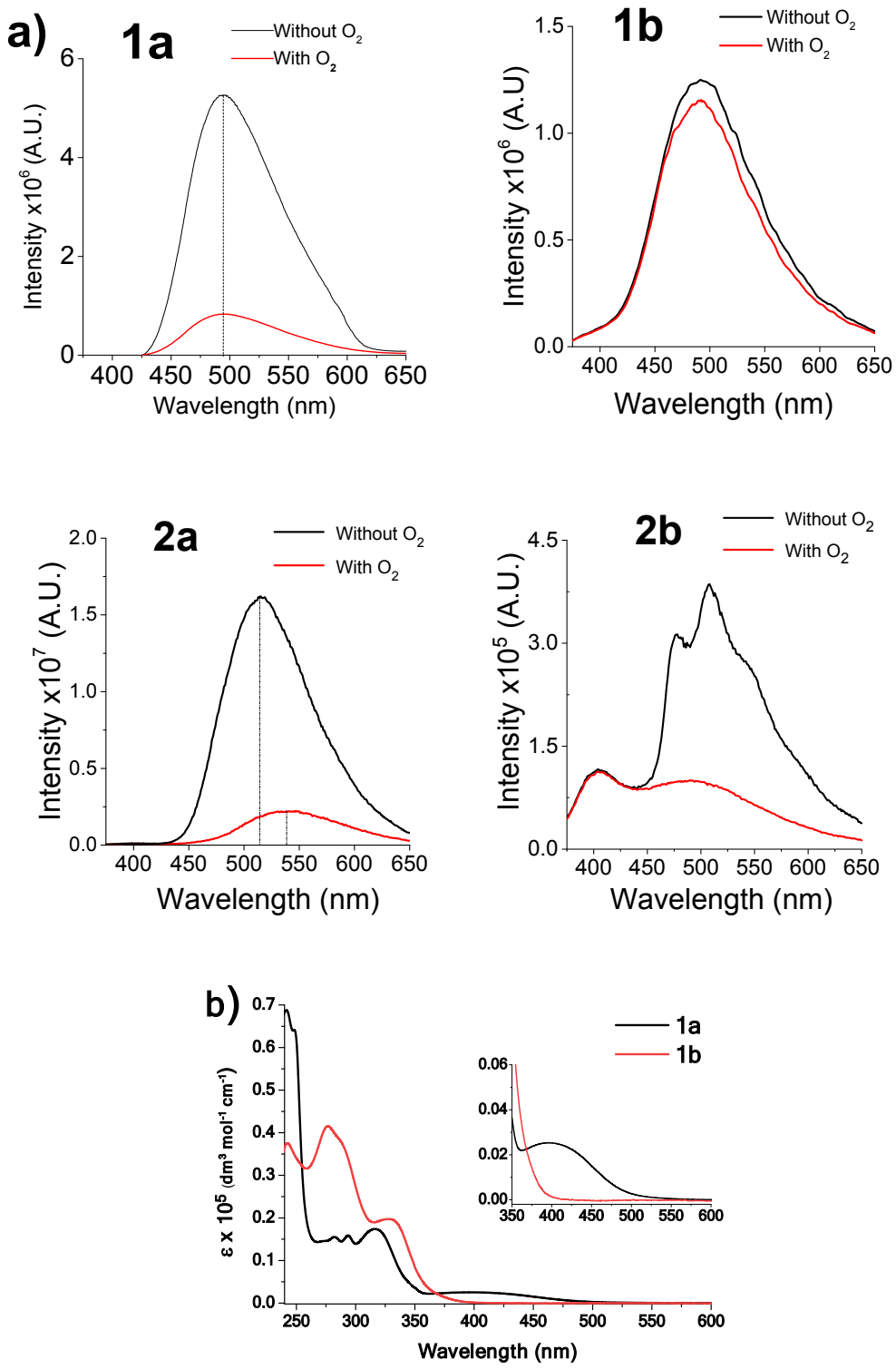

Figure 5. **a)** Steady state emission spectra for **1a**, **1b**, **2a** and **2b** in presence and absence of oxygen. All spectra are in zeonex matrix at 290 K. **b)** Absorption spectra for **1a-1b** in CH_2Cl_2 solution.

As ax-ax, ax-eq and eq-eq conformers are expected to be present for **1a**, **1b** and **2a** in zeonex, fully optimized excited state (S_1) geometries were located by TD-DFT computations here and their fluorescence ($S_0 \leftarrow S_1$) transition energies predicted. The geometries were optimized from their starting ground state (S_0) minima and distinct excited state (S_1) minima were located in most cases. The excited state geometries differ little from the ground state geometries for ax-ax conformers. However, they differ considerably for eq-ax and eq-eq conformers where the C(acceptor)-N bonds lengthen and C(donor)-N bonds shorten on going from S_0 to S_1 geometries (**Table S5**).

All these excited state minima revealed charge transfer (CT) character in the lowest energy emission where the ax-ax conformers contain little CT character and the eq-ax and eq-eq conformers have essentially pure CT character. These differences are shown pictorially in **Figure 6** where the hole and particle orbitals are located on the S_1 excited state geometries. The $S_0 \leftarrow S_1$ transition energies for the ax-ax conformers were consistently higher in energy (shorter wavelength) than the eq-ax and eq-eq conformers. As reported elsewhere, [36] the transitions are denoted as ^{1}CT(ax) and ^{1}CT(eq) respectively. Considering the likelihood of the conformers in zeonex films of the D-A-D systems here, ^{1}CT(eq) emissions would be observed in **1a**, **1b** and **2a**, whereas ^{1}CT(ax) emissions would be expected in **1b**, **2a** and **2b**.

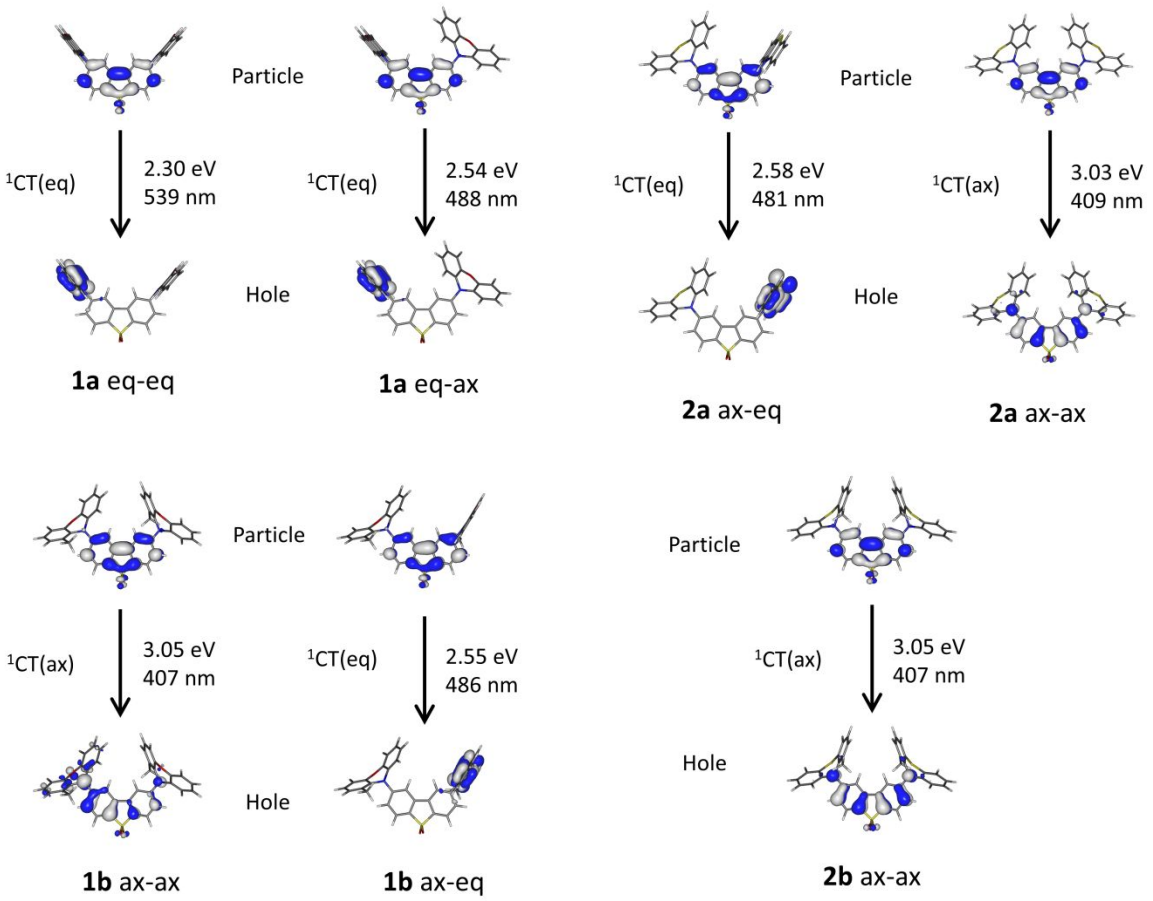

Figure 6. Orbitals involved in the $S_0 \leftarrow S_1$ fluorescence emissions and their emission energies on optimized excited state (S_1) geometries at the CAM-B3LYP/6-31G(d) level.

The emission band assignments for all four D–A–D systems were determined with the aid of time-jump emission data (**Figures 7**, **S5b–d**). CT (ax) and CT (eq) have different emission spectra and different lifetimes, with CT(eq) appearing at relatively longer wavelengths than CT(ax), and with longer lifetime, because it has stronger charge transfer character than CT(ax), induced by the near orthogonality between D and A units. CT(ax) and CT(eq) can thus be separated by collecting spectra at different time delays. Referring to the decay of **1b**: the emission in the temperature independent region appears with the CT(ax) spectrum, whereas the temperature dependent region, corresponding to TADF, is dominated by the

CT(eq) emission spectrum. This is also consistent with the fact that for compound **1a**, where TADF dominates, only CT(eq) emission is observed.

The emission spectrum for compound **1a** is essentially dominated by ^{1}CT(eq) prompt and delayed (TADF) fluorescence with negligible excitation (^{1}LE) emission contributions. The ^{1}LE fluorescence lifetime is very fast at less than 1 ns. The steady state spectrum for **1b** is more complex with at least three distinct fluorescence emissions, ^{1}LE, ^{1}CT(ax) and ^{1}CT(eq). The ^{1}CT(ax) transition is the dominant emission observed. The ^{1}LE fluorescence lifetime for **1b** is also very fast (< 1 ns) and the ^{1}CT(eq) emission band is observed at later times (ca 200 ns). The time difference is because ^{1}CT(eq) contributes to TADF unlike the ^{1}CT(ax) emission band.

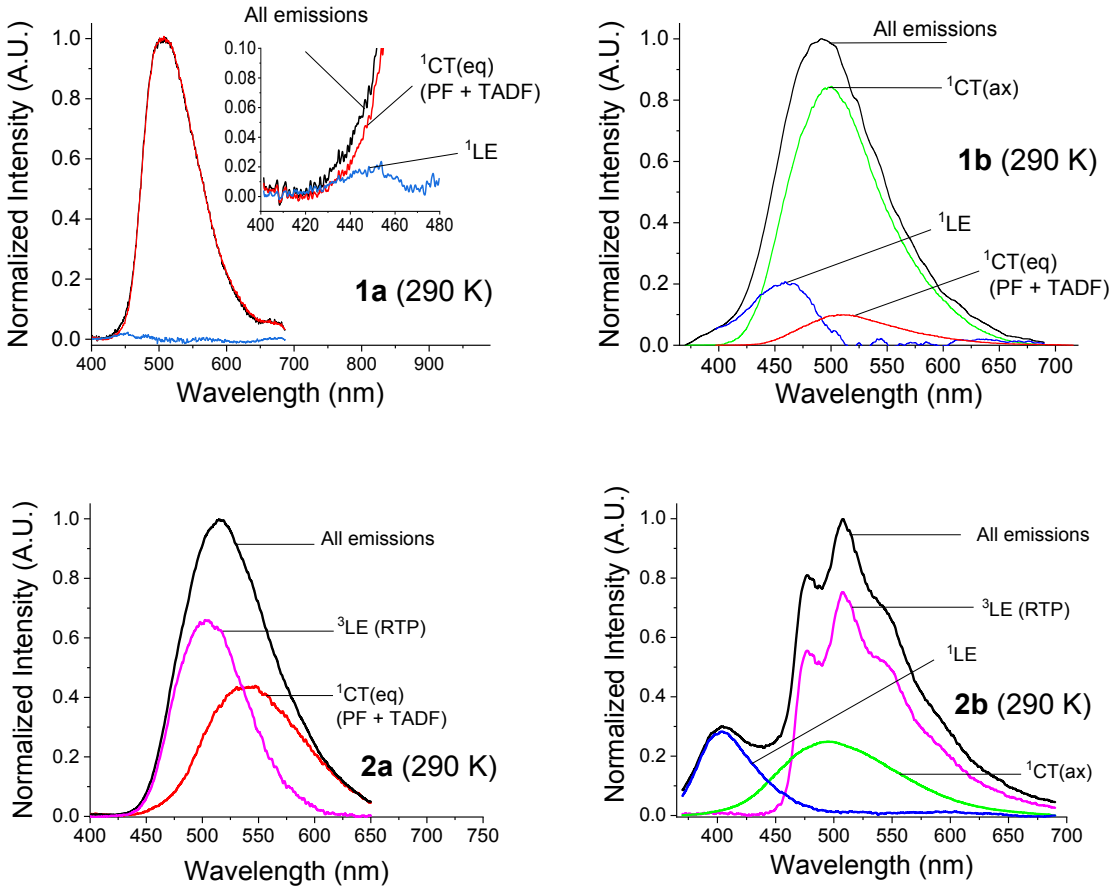

Figure 7. Proposed assignments of emission bands by fitting time-delay data within the steady state emission spectra ('all emissions') for **1a**, **1b**, **2a** and **2b**. Time-delay data are taken from figures in section **S5** and from literature data.[21,22]. As different species have different lifetimes they can be separated in the emission decay of **Figure S5a** using different decay times. This allows deconvolution of the emission of different species from the steady state 'all emissions' spectra. Then, these spectra are summed and combined in appropriate ratios to fit the steady-state emission spectrum. The time-jump emission components when added together fit very well under the 'all emissions' showing that all emissions have been separated and no contributions have been missed.

The emission spectra of the phenothiazines, **2a** and **2b**, are complicated by room temperature phosphorescence (RTP) present where the formally disallowed intersystem crossing (ISC) to triplet states is clearly promoted by the sulfur atoms. The time-delay data for **2a** show fast ^{1}LE fluorescence (*ca.* 1 ns) as a very small contribution to the overall emission intensity. Here there are two major contributions to the steady state emission spectrum of **2a** in the absence of oxygen, ^{1}CT(eq) and phosphorescence emissions. It is not clear from the time-delay data that any ^{1}CT(ax) emission exists. Since ax-ax conformers are expected to be present in zeonex for **2a**, it is presumed here that the observed RTP arises from the ax-ax conformers, whereas the observed ^{1}CT(eq) prompt and delayed fluorescence are from the ax-eq (and eq-eq) conformers. In the case of **2b** where only ax-ax conformers are expected in zeonex, the three distinct observed emissions must be ^{1}LE (with fast lifetimes at *ca.* 1 ns), ^{1}CT(ax) with lifetimes at 2-23 ns and RTP. The presence of RTP from ax-ax conformers of **2b** supports the assignment of RTP to the ax-ax conformers of **2a**.

Conclusions

A methyl group can be used to tune the emission properties of organic emissive molecules in distinctive ways beyond increasing electron donor strength. It can favor different conformers compared to unsubstituted D–A–D systems which then give very different CV data and photophysical properties. Through detailed calculations, it has been demonstrated that rotational barriers around D−A bonds in the

four D–A–D systems discussed herein are relatively low and therefore many different conformers are accessible at room temperature. The different conformers remain constrained in the solid state (zeonex) giving rise to multiple emissions such as local excitation fluorescence (^{1}LE), two distinct charge transfer (CT) fluorescence emissions depending on the axial (^{1}CT(ax)) or equatorial (^{1}CT(eq)) conformer, thermally activated delayed fluorescence (TADF from ^{1}CT(eq) only) and room temperature phosphorescence (^{3}LE, RTP from phenothiazines only) in the steady state emission spectra in the absence of oxygen. The data presented show that the phenoxazine derivative **1a** is the best TADF emitter molecule of the four D–A–D systems in zeonex matrix due to its preferential equatorial conformation. This detailed understanding of the steric, conformational and heteroatom effects should assist the rational design of new D–A–D systems with tunable optoelectronic properties. It is also now clear that the sulfur atom of phenothiazine plays a major role in RTP emission in this family of molecules.

Experimental Section

General experimental details

All reactions were carried out under an argon atmosphere. Starting materials were purchased commercially and were used as received. Solvents were dried using an Innovative Technology solvent purification system and were stored in ampoules under argon. TLC analysis was carried out using Merck Silica gel 60 F_{254} TLC plates and spots were visualized using a TLC lamp emitting at 365, 312 or 254 nm. Silica gel column chromatography was performed using silica gel 60 purchased from Sigma Aldrich. ^{1}H and ^{13}C NMR spectroscopy was carried out on Bruker AV400 and Varian VNMRS 700 spectrometers. Residual solvent peaks were referenced as described in the literature[42] and all NMR data was processed in MestReNova V11. Melting points were carried out on a Stuart SMP40 machine with a ramping rate of 4 $^{\circ}$C min^{-1}. Videos were replayed manually to determine the melting point. High resolution mass spectrometry was carried out on a Waters LCT Premier XE using ASAP ionisation. Samples were analyzed directly as solids. Elemental analysis was performed on an Exeter Analytical E-440 machine.

Any stated use of hexane refers to a mixed isomers grade. The same samples of molecule **1a**,[34] **2a**[22] and **2b**[21] from the literature were used for any additional measurements needed for comparison.

Cyclic voltammetry (CV) measurements were recorded at a scan rate of 100 mV s^{-1} at room temperature using an air-tight single-compartment three-electrode cell equipped with a glassy carbon working electrode (3 mm surface diameter), Pt wire counter electrode, and Pt wire pseudo-reference electrode. The cell was connected to a computer-controlled Autolab PG-STAT 30 potentiostat. The solutions contained the compound (1 mg/mL) and *n*-Bu_4NPF_6 (0.1 M) as the supporting electrolyte in dichloromethane (DCM) or dimethylformamide (DMF). All potentials were determined with the decamethylferrocene/decamethylferrocenium couple as an internal reference in DCM at −0.534 V or in DMF at −0.485 V for the usual reference standard of the ferrocene/ferrocenium couple (FcH/FcH^+) in DCM at 0.0 V. The current values in CV traces for **1b** and **2b** in the supporting information are in arbitrary units and adjusted to compare visually with **1a** and **2a** respectively for convenience. The HOMO and LUMO levels in **Table 1** were obtained from the onsets of the redox waves using the equations HOMO ≈ ionisation potential (IP) = $|e|(E_{ox}(onset)+5.1)$ eV and LUMO ≈ electron affinity (EA) = $-|e|(E_{red}(onset)+5.1)$ eV. The +5.1 V value is the ferrocenium/ferrocene couple potential.

All calculations were carried out with the Gaussian 09 package.[43] Ground state (S_0) geometries were fully optimized from different starting geometries using CAM-B3LYP with the 6-31(d) basis set.[44,45] Optimized geometries at the more computationally demanding model chemistry CAM-B3LYP/6-311G(d,p) did not give better agreement with experimental geometries than those at CAM-B3LYP/6-31G(d). The popular B3LYP[46] functional (and indeed many other pure/hybrid density functional theory (DFT) methods with zero/low Hartree-Fock (HF) wave contributions) is known to significantly underestimate charge transfer (CT) energies with respect to local excitation (LE) energies.[47] The CAM-B3LYP functional[48] is used here for more realistic relative energies between LE and CT as these emissions are observed experimentally. Unfortunately, the larger HF contribution in CAM-B3LYP means that all computed transition energies are vastly overestimated. Therefore, a simple scaling energy factor of

0.85 has been applied to all energies here for direct comparison with experimental data. All fully optimized S_0 geometries were found to be true minima based on no imaginary frequencies found from frequency calculations. The rotation energy profiles were constructed from partially optimized geometries where one C(donor)-N-C(acceptor)-C(acceptor) torsion angle is fixed at 5° intervals and each geometry optimization was carried out with the opt=modredundant command. The inversion energy barrier for each molecule (**1b**, **2a** or **2b**) was estimated from the energy of a planar N geometry by constraining the NC_4O or NC_4S ring to be planar and the geometry is partially optimized at the energy of the most stable fully optimized geometry. Time-dependent density functional theory (TD-DFT) calculations were carried out on the most stable minima of **1a** and **1b** at CAM-B3LYP/6-31G(d) to generate their simulated absorption spectra. Electronic structure calculations were carried out on selected minima to obtain the frontier orbital energies (HOMO/LUMO) for comparison with experimental values from CV measurements. The calculated optimized geometries and their energies are based on the gas-phase states. The calculated absolute energies and energy difference do not take into account intermolecular interactions present in the zeonex films, thus these calculated values should not be treated as quantitative. These quoted energies show that the CT(ax) emission is predicted to be higher in energy than the CT(eq) emission supporting our experimental evidence.

Singlet excited state (S_1) geometries were optimized using the td opt command from fully optimized S_0 geometries as starting geometries at CAM-B3LYP/6-31G(d). The $S_0 \leftarrow S_1$ transition energies were predicted from TD-DFT computations on the optimized S_1 geometries. Electronic structure calculations were performed on the optimized S_1 geometries to visualize the hole and particle orbitals. These are essentially the HOMO and LUMO orbitals as all $S_0 \leftarrow S_1$ transitions are dominated by these frontier orbitals (i.e. HOMO←LUMO). The MO figures were generated using the Gabedit package.[49] Natural transition orbitals (NTOs) were also generated and show virtually identical orbitals to the frontier orbitals (**Figure S6a**).

Thin films in zeonex were prepared by spin coating with guest:zeonex ratio of (1:20 *w/w*) from toluene solutions. Absorption and emission spectra were collected using a UV-3600 double beam spectrophotometer (Shimadzu), and a Fluorolog fluorescence spectrometer (Jobin Yvon). The extinction coefficient determination was performed in DCM solution. Some spectra in **Figure 7** were generated by simple subtractions of experimental spectra (including time-delay spectra) using Microsoft Excel. Phosphorescence, prompt fluorescence (PF), and delayed emission (DF) spectra and decays were recorded using nanosecond gated luminescence and lifetime measurements (from 800 ps to 1 s) with either a high energy pulsed Nd:YAG laser emitting at 355 nm (EKSPLA) or a N_2 laser emitting at 337 nm with pulse width 170 ps. Emission was focused onto a spectrograph and detected on a sensitive gated iCCD camera (Stanford Computer Optics) having sub-nanosecond resolution. PF/DF time resolved measurements were performed by exponentially increasing the gate and delay times. In general, time gated acquisition of luminescence signals is performed using increasing delay times, while the integration time is kept constant. The disadvantage in this method is that for weak signals, no luminescence can be measured at long-delay times with good S/N ratio. An alternative to this approach is to use increasing delay and integration times, so weak signals can be measured with good S/N ratio, as the integration time increases with delay time. The delay and integration times are chosen in a way that the next delay is set at a time longer than the previous delay+integration time. Therefore, no spectral overlap exists between the spectra corresponding to successive delays. The curve obtained directly from this process does not represent the real luminescence decay. However, this is easily corrected by integrating the measured spectra and dividing the integral by the corresponding integration time. In this way, each experimental point represents a snap-shot of the number of photons emitted per second at a time t = delay + (integration time)/2. The luminescence decay is then obtained by plotting each experimental point against time, and fitting with sum of exponentials. When required. In this way we are able to collect the entire emission spectrum decaying over 8 decades in time and in a single experiment. For initial development of these methods see previously published literature.[50] PLQY measurements were performed using a Quantaurus-QY Absolute PL quantum yield spectrometer using zeonex films prepared as described above.

X-ray diffraction experiments (**Table S6**) were carried out on a Bruker 3-circle D8 Venture diffractometer with a PHOTON 100 CMOS area detector, using Mo-K_α radiation from an Incoatec IμS microsource with focussing mirrors. Crystals were cooled to 120 K using a Cryostream (Oxford Cryosystems) open-flow N_2 gas cryostat. The structures were solved by direct methods using SHELXS 2013/1 software,[51] and refined by full-matrix least squares using SHELXL-2018 software[52] on OLEX2 platform.[53]

1-Methylphenoxazine (6)

This reaction is based on a modified literature procedure for other phenoxazine derivatives.[35] Phenoxazine **3** (1.00 g, 5.46 mmol, 1 eq.) was dried under high vacuum in a 50 mL 2-neck round-bottomed flask equipped with a stirrer bar for 30 min. The flask was back-filled with argon and dry THF (60 mL) was added *via* syringe. The reaction mixture was cooled to –78 °C and ^{n}BuLi (2.5 mL, 1.15 eq., 2.5 M in hexane) was added dropwise. The reaction mixture was stirred at –78 °C for 10 min and was allowed to warm to ambient temperature and was stirred for 20 min. The reaction was cooled to –78 °C and CO_2 was bubbled through the reaction mixture *via* cannula. The reaction mixture was warmed to ambient temperature and the solvent was slowly removed under reduced pressure to give a thick oily residue. The residue was redissolved in cold (–78 °C) dry THF (30 mL) *via* cannula transfer from a cooled ampoule. The reaction was cooled to –78 °C and ^{t}BuLi (3.2 mL, 1 eq., 1.7 M in hexane) was added dropwise. The reaction was allowed to warm to –15 °C and was stirred at this temperature for 1.5 h. The reaction mixture was cooled to –78 °C and MeI (774 mg/ 340 μL, 5.46 mmol, 1 eq.) was added dropwise. After 2 h at –78 °C, the reaction mixture was allowed to warm to ambient temperature and was stirred overnight. 1M HCl (100 mL) and then EtOAc (200 mL) were added to the reaction mixture and the organic layer was separated. The aqueous layer was extracted with EtOAc (2 × 200 mL). The organic extracts were combined and dried with $MgSO_4$ and were filtered. The solvent was removed under reduced pressure to give a crude oil which was purified by column chromatography eluting initially with hexane and then with gradient CH_2Cl_2/hexane 15 – 30% (*v*/*v*) in 5% increments. The title product was obtained as a brown

oil (645 mg, 60% yield). Note: The product contained ≈ 5% phenoxazine starting material which was removed in the next synthetic step.

^{1}H NMR (400 MHz, DMSO-d_6) δ 7.41 (s, 1H), 6.76 – 6.66 (m, 2H), 6.61 – 6.53 (m, 3H), 6.51 – 6.42 (m, 2H), 2.06 (s, 3H), ^{13}C{^{1}H} NMR (101 MHz, DMSO-d_6) δ 142.8, 142.6, 132.3, 130.2, 125.3, 123.6, 121.7, 120.5, 119.7, 114.8, 114.2, 112.8, 16.7; HRMS (ASAP^{+}-TOF) m/z: $[M+H]^{+}$ Calcd. for $C_{13}H_{12}NO$ 198.0913; Found: 198.0912.

2,8-Bis(1-methyl-phenoxazin-10-yl)dibenzothiophene-S,S-dioxide (1b)

2,8-dibromodibenzothiophene-*S,S*-dioxide[21,54] (274 mg, 0.73 mmol, 1 eq.) and 1-methylphenoxazine (**5**) (290 mg, 1.47 mmol, 2 eq.) were dried under vacuum for 30 min in a two-neck 100 mL round-bottomed flask fitted with a reflux condenser. The flask was back-filled with argon and dry toluene (18 mL) was added. The reaction mixture was bubbled with argon for 30 min, then $Pd_2(dba)_3 \cdot CHCl_3$ (38 mg, 37 μmol, 0.05 eq.) and $HP^tBu_3BF_4$ (21 mg, 73 μmol, 0.1 eq.) were added and the reaction mixture was bubbled with argon for a further 30 min. NaO^tBu (211 mg, 2.20 mmol, 3 eq.) was added under a high flow of argon and the reaction was then heated to 107 °C with stirring for 22 h. At the end of the reaction the solvent was removed under reduced pressure and the crude mixture was purified by column chromatography eluting with 80% CH_2Cl_2/hexane *v/v* switching to 100% CH_2Cl_2. Removal of solvent under reduced pressure gave product as a white solid (240 mg, 54% yield). The title compound was sublimed with heating (>300 °C) under high vacuum (9×10^{-2} mbar). Crystals of **1b** suitable for X-ray diffraction were obtained by vapour diffusion (vial in a vial) using $CDCl_3$ as solvent and 2,2,4-trimethylpentane as anti-solvent. Attempts with other alkane anti-solvents, such as pentane, hexane and heptane did not yield suitable crystals.

^{1}H NMR (400 MHz, $CDCl_3$) δ 7.55 (d, *J* = 8.5 Hz, 2H), 7.48 (dd, *J* = 7.6, 1.7 Hz, 2H), 7.30 – 7.18 (m, 8H), 7.11 – 7.05 (m, 4H), 7.03 – 7.01 (m, 2H), 6.99 (dd, *J* = 8.5, 2.3 Hz, 2H), 2.21 (s, 6H).^{13}C{^{1}H} NMR (176 MHz, $CDCl_3$) δ 154.3, 154.1, 152.1, 135.1, 133.5, 133.3, 131.1, 131.0, 127.3, 127.1, 126.8, 125.9,

123.5, 123.1, 118.0, 117.0, 115.6, 107.7,17.6; HRMS (ASAP$^+$-TOF) m/z: $[M+H]^+$ Calcd. for $C_{38}H_{27}N_2O_4S$ 607.1686; Found: 607.1678; Anal. Calc. for $C_{38}H_{26}N_2O_4S$: C, 75.23; H, 4.23; N. 4.62. Found: C, 75.51; H, 4.35; N, 4.59; m.p. decomp. > 330 °C.

Associated Content.

Supporting Information. ^1H and ^{13}C NMR spectra, absorption spectra, CV traces and data, additional emission data and computational data (PDF). CIF files for **1a** and **1b** have been deposited with the Cambridge Structural Database, CCDC-1568540 (**1a**) and 1568541 (**1b**).

Acknowledgements

J.S.W., F.B.D. and M.R.B. thank EPRSC for funding (Grant No. EP/L02621X/1). R.S.N. thanks the CAPES Foundation, Ministry of Education-Brazil (Grant No. BEX9474-13-7) for financial support.

References

(1) Zhang, D. D.; Cai, M. H.; Zhang, Y. G.; Zhang, D. Q.; Duan, L. Sterically shielded blue thermally activated delayed fluorescence emitters with improved efficiency and stability. *Mater. Horiz.* **2016**, *3*, 145-151.

(2) Chen, D. Y.; Liu, W.; Zheng, C. J.; Wang, K.; Li, F.; Tao, S. L.; Ou, X. M.; Zhang, X. H. Isomeric Thermally Activated Delayed Fluorescence Emitters for Color Purity-Improved Emission in Organic Light-Emitting Devices. *ACS Appl. Mater. Inter.* **2016**, *8*, 16791-16798.

(3) Li, Y. C.; Wang, Z. H.; Li, X. L.; Xie, G. Z.; Chen, D. C.; Wang, Y. F.; Lo, C. C.; Lien, A.; Peng, J. B.; Cao, Y.; Su, S. J. Highly Efficient Spiro[fluorene-9,9 '-thioxanthene] Core Derived Blue Emitters and Fluorescent/Phosphorescent Hybrid White Organic Light-Emitting Diodes. *Chem. Mater.* **2015**, *27*, 1100-1109.

(4) Echeverry, C. A.; Cotta, R.; Insuasty, A.; Ortiz, A.; Martin, N.; Echegoyen, L.; Insuasty, B. Synthesis of novel light harvesters based on perylene imides linked to triphenylamines for Dyes Sensitized Solar Cells. *Dyes Pigm.* **2018**, *153*, 182-188.

(5) Xiong, Y.; Wu, B.; Zheng, X. Y.; Zhao, Z.; Deng, P.; Lin, M.; Tang, B. Z.; Ong, B. S. Novel Dimethylmethylene-Bridged Triphenylamine-PDI Acceptor for Bulk-Heterojunction Organic Solar Cells. *Adv. Sci.* **2017**, *4*, 1700110.

(6) Hettiarachchi, S. U.; Prasai, B.; McCarley, R. L. Detection and Cellular Imaging of Human Cancer Enzyme Using a Turn-On, Wavelength-Shiftable, Self-Immolative Profluorophore. *J. Am. Chem. Soc.* **2014**, *136*, 7575-7578.

(7) Hou, X.; Ke, C.; Bruns, C. J.; McGonigal, P. R.; Pettman, R. B.; Stoddart, J. F. Tunable solid-state fluorescent materials for supramolecular encryption. *Nat. Commun.* **2015**, *6*, 6884.

(8) Gu, L.; Liu, R.; Shi, H.; Wang, Q.; Song, G.; Zhu, X.; Yuan, S.; Zhu, H. Synthesis, Luminescent Properties of aza-Boron-Diquinomethene Difluoride Complexes and Their Application for Fluorescent Security Inks. *J. Fluoresc.* **2016**, *26*, 407-412.

(9) Che, W.; Li, G.; Liu, X.; Shao, K.; Zhu, D.; Su, Z.; Bryce, M. R. Selective sensing of 2,4,6-trinitrophenol (TNP) in aqueous media with "aggregation-induced emission enhancement" (AIEE)-active iridium(iii) complexes. *Chem. Commun.* **2018**, *54*, 1730-1733.

(10) Li, X. C.; Wang, C. Y.; Wan, Y.; Lai, W. Y.; Zhao, L.; Yin, M. F.; Huang, W. A T-shaped triazatruxene probe for the naked-eye detection of HCl gas with high sensitivity and selectivity. *Chem. Commun.* **2016**, *52*, 2748-2751.

(11) Cai, Y.; Samedov, K.; Dolinar, B. S.; Albright, H.; Song, Z.; Zhang, C.; Tang, B. Z.; West, R. AEE-active cyclic tetraphenylsilole derivatives with approximately 100% solid-state fluorescence quantum efficiency. *Dalton Trans.* **2015**, *44*, 12970-12975.

(12) Kaji, H.; Suzuki, H.; Fukushima, T.; Shizu, K.; Suzuki, K.; Kubo, S.; Komino, T.; Oiwa, H.; Suzuki, F.; Wakamiya, A.; Murata, Y.; Adachi, C. Purely organic electroluminescent material realizing 100% conversion from electricity to light. *Nat. Commun.* **2015**, *6*, 8476.

(13) Kim, J. H.; Eum, M.; Kim, T. H.; Lee, J. Y. A novel pyrrolocarbazole donor for stable and highly efficient thermally activated delayed fluorescent emitters. *Dyes Pigm.* **2017**, *136*, 529-534.

(14) Zhang, D.; Zhao, C.; Zhang, Y.; Song, X.; Wei, P.; Cai, M.; Duan, L. Highly Efficient Full-Color Thermally Activated Delayed Fluorescent Organic Light-Emitting Diodes: Extremely Low Efficiency Roll-Off Utilizing a Host with Small Singlet-Triplet Splitting. *ACS Appl. Mater. Inter.* **2017**, *9*, 4769-4777.

(15) Yang, Z.; Mao, Z.; Xie, Z.; Zhang, Y.; Liu, S.; Zhao, J.; Xu, J.; Chi, Z.; Aldred, M. P. Recent advances in organic thermally activated delayed fluorescence materials. *Chem. Soc. Rev.* **2017**, *46*, 915-1016.

(16) Li, C.; Duan, R.; Liang, B.; Han, G.; Wang, S.; Ye, K.; Liu, Y.; Yi, Y.; Wang, Y. Deep-Red to Near-Infrared Thermally Activated Delayed Fluorescence in Organic Solid Films and Electroluminescent Devices. *Angew. Chem. Int. Ed.* **2017**, *56*, 11525-11529.

(17) Lee, I.; Lee, J. Y. Molecular design of deep blue fluorescent emitters with 20% external quantum efficiency and narrow emission spectrum. *Org. Electron.* **2016**, *29*, 160-164.

(18) Li, Y.; Xie, G.; Gong, S.; Wu, K.; Yang, C. Dendronized Delayed Fluorescence Emitters for Non-Doped, Solution-Processed Organic Light-Emitting Diodes with High Efficiency and Low Efficiency Roll-Off Simultaneously: Two Parallel Emissive Channels. *Chem. Sci.* **2016**, *7*, 5441-5447.

(19) Lin, T. A.; Chatterjee, T.; Tsai, W. L.; Lee, W. K.; Wu, M. J.; Jiao, M.; Pan, K. C.; Yi, C. L.; Chung, C. L.; Wong, K. T.; Wu, C. C. Sky-Blue Organic Light Emitting Diode with 37% External

Quantum Efficiency Using Thermally Activated Delayed Fluorescence from Spiroacridine-Triazine Hybrid. *Adv. Mater.* **2016**, *28*, 6976-6983.

(20) dos Santos, P. L.; Ward, J. S.; Bryce, M. R.; Monkman, A. P. Using Guest-Host Interactions To Optimize the Efficiency of TADF OLEDs. *J. Phys. Chem. Lett.* **2016**, *7*, 3341-3346.

(21) Ward, J. S.; Nobuyasu, R. S.; Batsanov, A. S.; Data, P.; Monkman, A. P.; Dias, F. B.; Bryce, M. R. The interplay of thermally activated delayed fluorescence (TADF) and room temperature organic phosphorescence in sterically-constrained donor-acceptor charge-transfer molecules. *Chem. Commun.* **2016**, *52*, 2612-2615.

(22) Dias, F. B.; Santos, J.; Graves, D. R.; Data, P.; Nobuyasu, R. S.; Fox, M. A.; Batsanov, A. S.; Palmeira, T.; Berberan-Santos, M. N.; Bryce, M. R.; Monkman, A. P. The Role of Local Triplet Excited States and D-A Relative Orientation in Thermally Activated Delayed Fluorescence: Photophysics and Devices. *Adv. Sci.* **2016**, *3*, 1600080.

(23) dos Santos, P. L.; Ward, J. S.; Congrave, D. G.; Batsanov, A. S.; Eng, J.; Stacey, J. E.; Penfold, T. J.; Monkman, A. P.; Bryce, M. R. Triazatruxene: A Rigid Central Donor Unit for a D–A_3 Thermally Activated Delayed Fluorescence Material Exhibiting Sub-Microsecond Reverse Intersystem Crossing and Unity Quantum Yield via Multiple Singlet–Triplet State Pairs. *Adv. Sci.* **2018**, *5*, 1700989.

(24) Huang, R. J.; Avo, J.; Northey, T.; Chaning-Pearce, E.; dos Santos, P. L.; Ward, J. S.; Data, P.; Etherington, M. K.; Fox, M. A.; Penfold, T. J.; Berberan-Santos, M. N.; Lima, J. C.; Bryce, M. R.; Dias, F. B. The contributions of molecular vibrations and higher triplet levels to the intersystem crossing mechanism in metal-free organic emitters. *J. Mater. Chem. C* **2017**, *5*, 6269-6280.

(25) Gibson, J.; Penfold, T. J. Nonadiabatic coupling reduces the activation energy in thermally activated delayed fluorescence. *Phys. Chem. Chem. Phys.* **2017**, *19*, 8428-8434.

(26) Etherington, M. K.; Gibson, J.; Higginbotham, H. F.; Penfold, T. J.; Monkman, A. P. Revealing the spin–vibronic coupling mechanism of thermally activated delayed fluorescence. *Nat. Commun.* **2016**, *7*, 13680.

(27) Gibson, J.; Monkman, A. P.; Penfold, T. J. The Importance of Vibronic Coupling for Efficient Reverse Intersystem Crossing in Thermally Activated Delayed Fluorescence Molecules. *ChemPhysChem* **2016**, *17*, 2956-2961.

(28) Samanta, P. K.; Kim, D.; Coropceanu, V.; Bredas, J. L. Up-Conversion Intersystem Crossing Rates in Organic Emitters for Thermally Activated Delayed Fluorescence: Impact of the Nature of Singlet vs Triplet Excited States. *J. Am. Chem. Soc.* **2017**, *139*, 4042-4051.

(29) Gan, S.; Luo, W.; He, B.; Chen, L.; Nie, H.; Hu, R.; Qin, A.; Zhao, Z.; Tang, B. Z. Integration of aggregation-induced emission and delayed fluorescence into electronic donor-acceptor conjugates. *J. Mater. Chem. C* **2016**, *4*, 3705-3708.

(30) Tanaka, H.; Shizu, K.; Miyazaki, H.; Adachi, C. Efficient green thermally activated delayed fluorescence (TADF) from a phenoxazine-triphenyltriazine (PXZ-TRZ) derivative. *Chem. Commun.* **2012**, *48*, 11392-11394.

(31) Higginbotham, H. F.; Yi, C. L.; Monkman, A. P.; Wong, K. T. Effects of Ortho-Phenyl Substitution on the rISC Rate of D-A Type TADF Molecules. *J. Phys. Chem. C* **2018**, *122*, 7627-7634.

(32) dos Santos, P. L.; Ward, J. S.; Batsanov, A. S.; Bryce, M. R.; Monkman, A. P. Optical and Polarity Control of Donor-Acceptor Conformation and Their Charge Transfer States in Thermally Activated Delayed Fluorescence Molecules. *J. Phys. Chem. C* **2017**, *121*, 16462-16469.

(33) Yang, J.; Zhen, X.; Wang, B.; Gao, X.; Ren, Z.; Wang, J.; Xie, Y.; Li, J.; Peng, Q.; Pu, K.; Li, Z. The influence of the molecular packing on the room temperature phosphorescence of purely organic luminogens. *Nat. Commun.* **2018**, *9*, 840.

(34) Chulkin, P.; Lapkowski, M.; Bryce, M. R.; Santos, J.; Data, P. Determination of standard redox rate constants of OLED active compounds by electrochemical impedance spectroscopy. *Electrochim. Acta* **2017**, *258*, 1160-1172.

(35) Katritzky, A. R.; Demiguel, L. M. V.; Rewcastle, G. W. Carbon-Dioxide - a Reagent for the Simultaneous Protection of Nucleophilic Centers and the Activation of Alternative Locations to Nucleophilic-Attack .13. Directed Synthesis of 1-Substituted Phenoxazines. *Heterocycles* **1987**, *26*, 3135-3140.

(36) Stockmann, A.; Kurzawa, J.; Fritz, N.; Acar, N.; Schneider, S.; Daub, J.; Engl, R.; Clark, T. Conformational control of photoinduced charge separation within phenothiazine-pyrene dyads. *J. Phys. Chem. A* **2002**, *106*, 7958-7970.

(37) Groom, C. R.; Allen, F. H. The Cambridge Structural Database in retrospect and prospect. *Angew. Chem. Int. Ed.* **2014**, *53*, 662-671.

(38) dos Santos, P. L.; Ward, J. S.; Data, P.; Batsanov, A. S.; Bryce, M. R.; Dias, F. B.; Monkman, A. P. Engineering the singlet-triplet energy splitting in a TADF molecule. *J. Mater. Chem. C* **2016**, *4*, 3815-3824.

(39) Golubev, V. A.; Tkachev, V. V.; Sen', V. D. Acid-catalyzed disproportionation of N,N-bis(4-tert-butylphenyl)hydroxylamine. Synthesis and structure of 10-[5-tert-butyl-2-(4-tert-butylphenylamino)phenyl]-3,7-di-tert-butylphenoxazine. *Russ. J. Org. Chem.* **2014**, *50*, 678-684.

(40) Huang, R.; Ward, J. S.; Kukhta, N. A.; Avó, J.; Gibson, J.; Penfold, T.; Lima, J. C.; Batsanov, A. S.; Berberan-Santos, M. N.; Bryce, M. R.; Dias, F. B. The influence of molecular conformation on the photophysics of organic room temperature phosphorescent luminophores. *J. Mater. Chem. C* **2018**, *6*, 9238-9247.

(41) Zhang, Z.; Gao, Y.; Liu, H.; Bai, Q.; Li, J. Y.; Liu, L. Q.; Wu, C. F.; Yang, B.; Wang, K.; Zou, B.; Wang, Y.; Lu, P. Dual fluorescence polymorphs: Wide-range emission from blue to red regulated by TICT and their dynamic electron state behavior under external pressure. *Dyes Pigm.* **2017**, *145*, 294-300.

(42) Fulmer, G. R.; Miller, A. J. M.; Sherden, N. H.; Gottlieb, H. E.; Nudelman, A.; Stoltz, B. M.; Bercaw, J. E.; Goldberg, K. I. NMR Chemical Shifts of Trace Impurities: Common Laboratory Solvents, Organics, and Gases in Deuterated Solvents Relevant to the Organometallic Chemist. *Organometallics* **2010**, *29*, 2176-2179.

(43) Frisch, M. J.; Trucks, G. W.; Schlegel, H. B.; Scuseria, G. E.; Robb, M. A.; Cheeseman, J. R.; Scalmani, G.; Barone, V.; Mennucci, B.; Petersson, G. A.; Nakatsuji, H.; Caricato, M.; Li, X.; Hratchian, H. P.; Izmaylov, A. F.; Bloino, J.; Zheng, G.; Sonnenberg, J. L.; Hada, M.; Ehara, M.; Toyota, K.; Fukuda, R.; Hasegawa, J.; Ishida, M.; Nakajima, T.; Honda, Y.; Kitao, O.; Nakai, H.; Vreven, T.; Montgomery, J. A., Jr.; ; Peralta, J. E.; Ogliaro, F.; Bearpark, M.; Heyd, J. J.; Brothers, E.; Kudin, K. N.; Staroverov, V. N.; Kobayashi, R.; Normand, J.; Raghavachari, K.; Rendell, A.; Burant, J. C.; Iyengar, S. S.; Tomasi, J.; Cossi, M.; Rega, N.; Millam, J. M.; Klene, M.; Knox, J. E.; Cross, J. B.; Bakken, V.;

Adamo, C.; Jaramillo, J.; Gomperts, R.; Stratmann, R. E.; Yazyev, O.; Austin, A. J.; Cammi, R.; Pomelli, C.; Ochterski, J. W.; Martin, R. L.; Morokuma, K.; Zakrzewski, V. G.; Voth, G. A.; Salvador, P.; Dannenberg, J. J.; Dapprich, S.; Daniels, A. D.; Farkas, Ö.; Foresman, J. B.; Ortiz, J. V.; Cioslowski, J.; Fox, D. J. Gaussian 09, Revision A.02. *Gaussian, Inc Wallingford CT* **2009**.

(44) Petersson, G. A.; Bennett, A.; Tensfeldt, T. G.; Allaham, M. A.; Shirley, W. A.; Mantzaris, J. A Complete Basis Set Model Chemistry .1. The Total Energies of Closed-Shell Atoms and Hydrides of the 1st-Row Elements. *J. Chem. Phys.* **1988**, *89*, 2193-2218.

(45) Petersson, G. A.; Allaham, M. A. A Complete Basis Set Model Chemistry .2. Open-Shell Systems and the Total Energies of the 1st-Row Atoms. *J. Chem. Phys.* **1991**, *94*, 6081-6090.

(46) Becke, A. D. Density-Functional Thermochemistry .3. The Role of Exact Exchange. *J. Chem. Phys.* **1993**, *98*, 5648-5652.

(47) Dreuw, A.; Weisman, J. L.; Head-Gordon, M. Long-range charge-transfer excited states in time-dependent density functional theory require non-local exchange. *J. Chem. Phys.* **2003**, *119*, 2943-2946.

(48) Yanai, T.; Tew, D. P.; Handy, N. C. A new hybrid exchange-correlation functional using the Coulomb-attenuating method (CAM-B3LYP). *Chem. Phys. Lett.* **2004**, *393*, 51-57.

(49) Allouche, A. R. Gabedit-A Graphical User Interface for Computational Chemistry Softwares. *J. Comput. Chem.* **2011**, *32*, 174-182.

(50) Rothe, C.; Monkman, A. P. Triplet exciton migration in a conjugated polyfluorene. *Phys. Rev. B* **2003**, *68*, 075208.

(51) Sheldrick, G. M. A short history of SHELX. *Acta Crystallogr. A* **2008**, *64*, 112-122.

(52) Sheldrick, G. M. Crystal structure refinement with SHELXL. *Acta Crystallogr. C Struct. Chem.* **2015**, *71*, 3-8.

(53) Dolomanov, O. V.; Bourhis, L. J.; Gildea, R. J.; Howard, J. A. K.; Puschmann, H. OLEX2: a complete structure solution, refinement and analysis program. *J. Appl. Crystallogr.* **2009**, *42*, 339-341.

(54) Gilman, H.; Nobis, J. F. Rearrangement with 4-Iododibenzothiophene in Amination by Sodamide. *J. Am. Chem. Soc.* **1945**, *67*, 1479-1480.